

Crystallinity of dsRNA-AMP complexes modulates TLR3-mediated inflammation

Ernest Y. Lee¹, Toshiya Takahashi², Tine Curk^{3,4}, Jure Dobnikar^{3,4,5*}, Richard L. Gallo^{2*}, Gerard C. L. Wong^{1*}

¹ Department of Bioengineering, University of California, Los Angeles, Los Angeles, CA 90095, United States

² Department of Dermatology, University of California, San Diego, La Jolla, CA 92093, United States

³ Department of Chemistry, University of Cambridge, Cambridge, UK

⁴ Beijing National Laboratory for Condensed Matter Physics & CAS Key Laboratory of Soft Matter Physics, Institute of Physics, Chinese Academy of Sciences, Beijing 100190, China

⁵ School of Physical Sciences, University of Chinese Academy of Sciences, Beijing 100049, China

*To whom correspondence should be addressed:

Gerard C.L. Wong

Department of Bioengineering, University of California, Los Angeles, 4121 Engineering V UCLA
Los Angeles, CA 90095. Tel: (310) 794-7684 Email: gclwong@seas.ucla.edu

Richard L. Gallo

Department of Dermatology, University of California, San Diego, 3350 La Jolla Village Drive, San Diego, CA 92161. E-mail address: rgallo@ucsd.edu

Jure Dobnikar

Department of Chemistry, University of Cambridge, Cambridge, UK
Email address: jd489@cam.ac.uk

Abstract

Double-stranded RNA (dsRNA) induces production of pro-inflammatory cytokines in normal human epidermal keratinocytes (NHEK) by specific binding to endosomal Toll-like receptor-3 (TLR3). Recently, it has been shown that hyperactivation of TLR3 in psoriatic keratinocytes by dsRNA can occur in the presence of human antimicrobial peptide (AMP) LL37. Here, we combine synchrotron X-ray scattering, microscopy, computer simulations, and measurements of NHEK cytokine production to elucidate a previously unanticipated form of specific molecular pattern recognition. LL37 and similar α -helical AMPs can form proinflammatory nanocrystalline complexes with dsRNA that are recognized by TLR3 differently than dsRNA alone. dsRNA complexes that activate IL-6 production in NHEK and those that do not are both able to enter cells and colocalize with TLR3. However, the crystallinity of these AMP-dsRNA complexes, specifically the geometric spacing between parallel dsRNA and the repeat number of ordered dsRNA, strongly influence the level of TLR3 activation. Crystalline complexes that present dsRNA at a spacing that matches with the steric size of TLR3 can recruit and engage multiple TLR3 receptors, driving receptor clustering and immune amplification, whereas crystalline complexes that exhibit poor steric matching do not. Reverse-transcription quantitative PCR (RTqPCR) of IL-6 during siRNA knockdown of TLR3 confirms that cytokine

production is due to TLR3: High levels of IL-6 transcription are observed for sterically-matched complexes without TLR3 knockdown, whereas such activity is abrogated with TLR3 knockdown. Computer simulations show that TLR3 binding and activation is more forgiving for complexes with spacings that are sterically larger than the receptor, in agreement with experiments.

Significance Statement

Double-stranded RNA (dsRNA) complexes with antimicrobial peptides (AMPs) potentially activate Toll-like receptor 3 (TLR3), leading to exacerbation of inflammation in autoimmune diseases such as psoriasis. At present, it is not clear whether immune activation by single ligands vs. complexes of ligands are different, or how the latter may lead to immune amplification. By using small-angle X-ray scattering, direct immunological measurements, and computer simulations, we show the counterintuitive result that the crystallinity of these complexes can enforce qualitatively different immune outcomes. In fact, the specific inter-dsRNA spacing between parallel dsRNA ligands in the complex and the average number of dsRNA presented by ordered crystalline domains to TLR3 receptors both quantitatively influence immune activation.

Keywords (3-5): dsRNA, Toll Like Receptors, psoriasis, antimicrobial peptides, innate immunity

\body

TLR3 recognition of dsRNA is a fundamental example of molecular recognition (1). Binding of viral dsRNA to TLR3 in endosomes triggers downstream NF- κ B activation and production of pro-inflammatory cytokines (2, 3). Recently, non-coding host-derived dsRNA has also been shown to break immune tolerance and activate TLR3, but these dsRNAs require presence of the antimicrobial peptide (AMP) LL37 (4). Interestingly, in psoriasis, self-dsRNA can complex with LL37, access endosomes, potentially activate TLR3 in keratinocytes (5-8) and amplify production of the pro-inflammatory cytokines IL-6 and IFN- β (9), thereby exacerbating disease (10). A variety of RNA-binding proteins (11, 12), AMPs (13), cell-penetrating peptides (14), cationic lipids (15), and synthetic polymers (16) have also been reported to bind to dsRNA. Electrostatic complexes between anionic polymers and cationic molecules are stabilized by the entropy gain of counterion release (17) and have been studied extensively (17-23). However, the structures of dsRNA complexes with immunologically relevant polycations, many of which are amphiphilic and impart an additional principle of self-assembly, are largely unknown. Importantly, it is unclear which of these self-assembled dsRNA complexes induce immune responses and which do not. A common hypothesis explaining the ability of complexed nucleic acids to activate endosomal immune receptors is that formation of aggregates confers increased efficiency of endosomal access and protection from nuclease degradation (24). Although this model can explain why self-antigens can activate TLRs, it does not explain why some complexes are pro-inflammatory while others are non-inflammatory. Recent results on activation of TLR9 by dsDNA complexes suggest that cooperativity of ligand binding may be important (25), but it is not clear whether these results are generalizable. At present, the mechanism for TLR3 activation by polycation-dsRNA complexes is not well understood.

It is not surprising that anionic dsRNA and cationic molecules (ex: AMPs) can form electrostatic complexes. Perhaps a little more surprising is the observation that polycation-dsRNA complexes that activate IL-6 production and those that do not are both able to enter cells efficiently and colocalize with endosomal TLR3 in normal human epidermal keratinocytes (NHEK), which shows that the ability to access endosomal compartments, a necessary condition of activation, is not the only determinant for strong immune activation. What is unanticipated is the discovery against expectation that TLR3 immune activation depends strongly on the recognition of crystallinity in dsRNA-AMP complexes, and metrics of crystalline order can drive immune outcomes. The two major criteria defining TLR3 activation and amplification are 1) the inter-dsRNA spacing between parallel dsRNA ligands within the dsRNA complex, and 2) the average size (the average number of unit cells) of ordered crystalline domains within dsRNA complexes. These criteria, the lattice constant and the domain size, correspond to two fundamental measures of crystallinity. We rationalize this behavior using a coarse-grained computational model and show that TLR3 binding to dsRNA is optimized when the inter-dsRNA spacings are in an optimum range: Crystalline complexes that present dsRNA at a spacing well-matched with the TLR3 steric size can recruit and engage multiple TLR3 receptors, effectively driving receptor clustering and immune amplification, whereas complexes that exhibit poor steric matching do not. Our observations are consistent with a conceptual framework in which activation levels are modulated by different inter-RNA spacings and by different crystalline RNA domain sizes in AMP-dsRNA complexes. Importantly, reverse-transcription quantitative PCR (RTqPCR) of IL-6 during siRNA knockdown of TLR3 confirms that observed cytokine production is

due to TLR3: High levels of IL-6 transcription are observed for sterically-matched complexes without knockdown, whereas abrogation of such activity is observed for these complexes with TLR3 knockdown. Recent work on TLR9 has shown that complexes between dsDNA and polycations at optimal inter-DNA spacings (such as LL37) can lead to a drastic increase of interferon- α secretion by plasmacytoid dendritic cells, whereas those at mismatched spacings do not (25). Taken together with the evidence adduced here, these cognate observations suggest that AMP-induced ligand clustering and crystalline ordering can lead to an unexpected channel of pattern recognition and amplification for TLR responses, and a potentially general mode of AMP immunomodulatory function.

Results and Discussion

IL-6 production in keratinocytes through TLR3 activation depends on the inter-dsRNA spacing within self-assembled polycation-dsRNA electrostatic complexes

The structural basis of dsRNA binding by TLR3 has been demonstrated via X-ray crystallography (26) (Figure 1A). dsRNA can bind electrostatically via the anionic phosphate backbone to cationic portions of TLR3 dimers. Since complexes of dsRNA and various cationic molecules can lead to high levels of immune activation (27), we investigate their structures. To assess the relationship between keratinocyte activation and these peptide-dsRNA complexes, we characterized 15 polycation-dsRNA structures with SAXS and correlated these structures with their ability to activate NHEK cells. Consistent with the behavior of other electrostatic complexes composed of nucleic acids (28), the observed structures do not depend strongly on the global concentration of these complexes. The structures of these complexes, however, can in principle change with the composition of the complex. To mitigate this uncertainty, we solved each individual structure at three or more different polycation-to-dsRNA molar ratios on both sides of the isoelectric point, the stoichiometry at which the negative charge of the dsRNA is compensated by the positive charge of the polycation (typically obtained from the polycation to dsRNA charge ratio, $P/RNA = 1/4, 1/2, 1/1, 2/1, 4/1$). This library of over 50 solved structures, which covers a large range of physiologically relevant scenarios, is organized into a “phase diagram” for each type of complex. We find that the self-assembled structures of these dsRNA complexes are remarkably conserved for a broad range of stoichiometry with minor exceptions. Typical structures are dsRNA columnar phases with different in-plane symmetries (square lattices, hexagonal lattices, disordered lattices), and with different spacings between dsRNA (center-to-center distances between dsRNA). From each structure, we measure the inter-dsRNA spacing a , the linear domain size L (and the repeat number m) (Table S1). Details are found in the Supplementary Information.

To assess the level of immune activation induced by each complex, IL-6 protein production is measured as a quantitative readout for NHEK activation using ELISA (Table S1). The data shows that some dsRNA complexes strongly amplify TLR3 activation while others do not. To investigate the origin of this difference, we compare the measured level of IL-6 production with the inter-dsRNA spacing and unit cell repeat number of each complex for each set of stoichiometric conditions in our phase diagram. We find that there is a strong relationship between the structure of polycation-dsRNA immune complexes and their ability to amplify IL-6 production. Specifically, immune complexes with inter-dsRNA spacings much smaller than TLR3

do not activate strongly (Figure 1B), while complexes with inter-dsRNA spacings roughly commensurate with the size of TLR3 maximize activation (Figure 1C). We have chosen to illustrate these differences by highlighting four prototypical examples of polycation-dsRNA complexes with varying structures. HIV-TAT is a well-characterized cell-penetrating peptide that has been explored as a nucleic acid transfection reagent, and is known to have strong endosomal access (29, 30). Buforin is an antimicrobial peptide obtained from a histone fragment that is known to penetrate cell membranes and bind to nucleic acids (31, 32). Spermine is an endogenous polyamine known to be biologically important in the folding and binding of nucleic acids to their targets (33-35), and is a structural relative of many cationic polymers used for gene delivery applications. LL37 is a multifunctional endogenous innate immunity peptide that is implicated in the pathogenesis of autoimmune disease such as lupus and psoriasis (24, 36, 37). It can also form pores in membranes, enable endosomal access, and has been reported to signal to the immune system via TLR9 (38).

From SAXS measurements, the TAT-dsRNA complex forms a close-packed 3D hexagonal columnar lattice with a first peak position at $q_{100} = 0.217 \text{ \AA}^{-1}$ and higher order reflections at $q_{001} = 0.271$, $q_{110} = 0.384$, and $q_{200} = 0.441 \text{ \AA}^{-1}$, corresponding to an inter-dsRNA spacing of $a \sim 2.90$ nm, which is much smaller than the steric size of TLR3 (Figure 1B, 1D). In contrast, the structure of the buforin-dsRNA complex is an “open” 2D hexagonal columnar lattice with a first peak position at $q_{10} = 0.182 \text{ \AA}^{-1}$ and higher order reflections at $q_{11} = 0.314 \text{ \AA}^{-1}$, $q_{20} = 0.362 \text{ \AA}^{-1}$, and $q_{21} = 0.482 \text{ \AA}^{-1}$, corresponding to a larger inter-dsRNA spacing of $a \sim 3.45$ nm that can accommodate the size of TLR3 (Figure 1C, 1D). dsRNA complexes based on TAT induce low levels of IL-6 even though TAT is known to exhibit pervasive endosomal access in a broad range of cells. In comparison, dsRNA complexes based on buforin exhibits high levels of IL-6 production, with the latter inducing an order of magnitude ($\sim 10\times$) more IL-6 production than TAT-dsRNA complexes (Figure 1E). SAXS measurements show that spermine-dsRNA complexes form tightly packed hexagonal columnar arrays, corresponding to an inter-dsRNA spacing of $a \sim 2.69$ nm (Figure 2A, 2B). In contrast, LL37-dsRNA complexes exhibited a single diffraction peak at $q_1 = 0.173 \text{ \AA}^{-1}$ corresponding to an average inter-dsRNA spacing of 3.63 nm, consistent with an “open” disordered columnar complex (Figure 2A, 2C). Like buforin, LL37-dsRNA complexes induce high levels of IL-6 production from NHEK, consistent with prior experimental observations (27), but spermine-dsRNA complexes, like TAT-dsRNA complexes, do not. Quantitatively, complexes based on LL37 induce $\sim 5\times$ more IL-6 from NHEK than those based on spermine. The disparity between IL-6 expression levels induced by LL37- and buforin-dsRNA with those induced by TAT- and spermine-dsRNA complexes illustrate two distinct families of structures that differentially predict immune activation (Figure 1B, 1C, 2C). In fact, our immune activation data for the 15 different dsRNA complexes suggest that the measured inter-dsRNA spacings in these complexes correlate strongly with TLR3 activation (Figure 1E). Using nonlinear correlations and bootstrapping analyses, we find that there is a statistically significant relationship between TLR3 activation and inter-RNA spacing (see SI discussion and Figure S1). Generally, we observed that complexes with first peak positions $\sim 1.7\text{-}1.9 \text{ nm}^{-1}$ strongly activated TLR3, while those outside this range had reduced abilities to activate TLR3. We note that although most complexes follow the trend line, a small subset of complexes appears to deviate slightly. This is not surprising given the complex nature of TLR activation: For example, it is possible that small quantitative differences in the degree of endosomal access between different types of dsRNA-peptide complexes can influence

the level of the IL-6 response. In particular, from our previous SAXS experiments with model membranes, LL37, CRAMP, and their mutants exhibit different levels of membrane curvature generating activity due to differences in charge, hydrophobicity, and amphipathicity, which can alter their intake pathways and thereby TLR access. Differential degradation rates of these peptides in biological environments may also play a role in the observed variation. In fact, our characterization of the structures of a cohort of LL37 fragments bound to dsRNA mimics the distribution of LL37 degradation products likely present *in vivo*.

Cytokine-inducing polycation-dsRNA complexes activate NHEK via TLR3

From the data in Figure 1E, we observed that IL-6 amplifying and non-IL-6-amplifying molecules activate TLR3 to varying degrees. To assay whether polycation-dsRNA complexes indeed co-localize with and activate specifically through TLR3, we carried out fluorescence microscopy experiments and RTqPCR experiments with NHEK. We tested one IL-6 amplifying complex (LL37) and two non-amplifying complexes (TAT and spermine). From microscopy studies of prototypical examples of dsRNA-polycation complexes, we find that dsRNA complexes that amplify NHEK production of IL-6 and those that do not both enter cells and colocalize with TLR3 (Figure 3A). Interestingly, LL37-dsRNA, TAT-dsRNA, and spermine-dsRNA all enter NHEK cells and apparently bind to TLR3. However, only LL37-dsRNA complexes seem to amplify cytokine production, while the other complexes do not. These results suggest that internalization and access to immune cells, while clearly important to be sure, do not by themselves explain differences in levels of immune activation. Entry and binding to TLR3 is necessary but not sufficient for immune amplification. Rather, the inter-dsRNA spacing appears to play an important role also. To confirm that the cytokine production is indeed specifically due to TLR3, we conducted RTqPCR of IL-6 during siRNA knockdown of TLR3 in the presence and absence of the complexes. We observe high levels of IL-6 transcription for IL-6-amplifying LL37-dsRNA, Peptide 2-dsRNA, and buforin-dsRNA complexes without knockdown, and the abrogation of such activity with TLR3 knockdown, suggesting that activation of TLR3 by these complexes directly leads to cytokine production (Figure 3B) ($p^* < 0.05$ for dsRNA only, $p^{***} < 0.001$ for buforin-dsRNA, $p^{**} < 0.01$ for Peptide 2-dsRNA, $p^* < 0.05$ for LL37-dsRNA). To confirm that the siTLR3 indeed knocked down TLR3 expression, we also measured TLR3 expression via RTqPCR (Figure 3C) ($p < 0.001$). Although it is generally recognized that siRNA knockdown is not always completely efficient, we observe significant knockdown of IL-6 transcription. We note that it is possible that some residual IL-6 production may be present due to endosomal escape and activation of the cytoplasmic MAVS signaling pathway by dsRNA complexes. In summary, IL-6 induction by polycation-dsRNA complexes are mediated at least in part by TLR3, and maximally-inducing complexes exhibit similar degrees of endosomal access as non-amplifying complexes.

Coarse-grained model of TLR3 binding to RNA bundles exhibits dependence on inter-dsRNA spacing and repeat number in agreement with experimental observations

To investigate TLR3 interactions with ordered dsRNA immune complexes, we developed a coarse-grained theoretical model, which aims to predict the fraction of ligand-bound, active TLR3 receptors $f_A(q, m)$ as a function of the crystallinity parameters $q = 2\pi/a$ (where a is the inter-dsRNA spacing) and m (repeat number of RNA in the complex) (Figure 4A). Experimentally, the repeat number m is calculated from the linear domain size L (see Supplementary Information).

The dsRNA complex/TLR3 system is cognate to the dsDNA complex/TLR9 system, which we have previously engaged (25). Based on crystallography data, TLR3 (26) has a larger opening angle compared to TLR9 (39). Therefore, we predict that the optimal lattice spacing resulting in maximal TLR3 activation will be larger for RNA-peptide complexes compared to DNA-peptide complexes. That dsRNA complexes exhibit different domain sizes affords us the opportunity to explicitly take into consideration the effect of varying the repeat number of polycation-dsRNA complexes on TLR3 activation, in addition to the inter-dsRNA spacing. We also take into account the variable strength of the TLR3-dsRNA backbone interactions and explicitly include the density of TLR3 in the endosome and average dsRNA length. To do this, we use a Langmuir-like approach and assume that there are k possible binding sites for TLR3 receptors on each dsRNA cluster (i.e. k is the maximum number of TLR3 receptors that can bind to each peptide-dsRNA cluster), with all binding sites identical and independent. The number k is determined by the repeat number m and the individual dsRNA length. Here, the TLR3 receptor molecules interact only through the hard-core excluded volume interaction forbidding their overlap. The total number of bound TLR3 is given by a Langmuir isotherm $n_B = k \frac{(1-f_A)e^{-\varepsilon(a)/k_B T}}{1+(1-f_A)e^{-\varepsilon(a)/k_B T}}$.

The single TLR3 binding free energy $\varepsilon(a) = \Delta G + \mu^{TLR} + 2U(a)$ includes 3 terms: the “pure” TLR3-dsRNA Gibbs interaction free energy ΔG , the concentration independent part of the chemical potential μ^{TLR} of TLR3 in the endosomal membrane, and the backbone electrostatic interaction $U(a)$ due to the presence of adjacent anionic RNA rods in a cluster with spacing a . (25). The terms $\varepsilon^* = \Delta G + \mu^{TLR}$ and will be treated as a constant parameter. We also explicitly consider receptor depletion captured by a factor $(1 - f_A)$, with f_A denoting the fraction of all bound (activated) receptors. More bound TLR3 leads to fewer available TLR3, increasing the cost of recruitment. The fraction of all active receptors is $f_A = \frac{n_B N_c}{N^{tot}}$, with N_c the average number of clusters on the membrane and N^{tot} the total number of TLR3 receptors. Assuming equilibrium between clusters in solution and those adsorbed to a membrane, we can determine f_A using a self-consistent relationship from multivalent adsorption theory (25, 40, 41) (see SI Eqn 3).

In Figure 4B, we present a contour plot of the fraction of active TLR3 receptors f_A (and predicted immune activation profile) as a function of the first peak position q and the repeat number m with $B = 30k_B T$ and interaction energy $\varepsilon^* = 2k_B T$ (a contour plot showing the fraction of active TLR3 receptors as function of the interaction strength ε and repeat number m is found in Figure S2). We assume that f_A is a good proxy for TLR3 activation and IL-6 production, with a larger fraction of active receptors correlating with increased immune activation and cytokine secretion. Using the approximate model here, a strong dependence on the inter-dsRNA spacing is observed. Moreover, a dependence on the repeat number m is also clearly observed. At larger m , dsRNA complexes with a broader range of inter-dsRNA spacings can maximally activate TLR3, while at smaller m , a narrower range of spacing is allowed (Figure S3A). At an inter-dsRNA spacing that is highly commensurate (well-matched) with the steric size of TLR3, even relatively small ligand clusters with a low number of repeats m can significantly activate due to strong multivalency and resultant “superselective” effects (40, 41). Interestingly, at spacings slightly larger than the steric size, a large m can compensate for reduced effective binding energy between sterically-mismatched dsRNA ligands and TLR3 (Figure S3B), while at spacings smaller than the steric size this is not possible. These observations suggest that the elastic response of dsRNA-AMP nanocrystals to deformations can influence binding to TLR3 and thereby immune

activation. For spacings much larger or smaller than the TLR3 size, we observe a sharp drop in number of bound TLR3 ($q > 2.0 \text{ nm}^{-1}$). This trend is reflected in the experimental data: polycation-dsRNA clusters with small inter-dsRNA spacings ($q > 2.0 \text{ nm}^{-1}$) like HIV-TAT and spermine cannot potentiate TLR3 activation despite having a large domain size ($L \sim 17 \text{ nm}$ for both TAT and spermine). In contrast, buforin-dsRNA and LL37-dsRNA complexes have quite different domain sizes and number of repeats, but since both have ideal inter-dsRNA spacing, they both activate NHEK. The buforin complex has a larger repeat number m than the LL37 complex (Table S1), explaining the higher relative levels of IL-6 induction by buforin-dsRNA. Indeed, in Figure 4C, we show that the fraction of active TLR3 receptors f_A can be predicted from both the experimentally measured inter-dsRNA spacing and the repeat number m , and that there is good correspondence between the model (black) and experimentally measured IL-6 secretion (red, data reproduced from Figure 1E).

To understand how the fraction of activated TLR3 depends on the crystallinity of TLR3-AMP complexes, we conducted coarse-grained Grand canonical Monte-Carlo simulations on TLR3-dsRNA binding (details in Supplementary Information). The fraction of bound and activated TLR3 receptors f_A for multiple dsRNA-AMP complexes with varying inter-dsRNA spacings a is calculated. In Figure 4D, simulation results for f_A vs $q = 2\pi/a$ are shown for parameters $B = 30k_B T$ and $m = 4$. For an interaction energy of $\epsilon = 3 k_B T$, the fraction of active TLR3 is maximized for complexes with 1st order diffraction peaks near $q \sim 1.85 \text{ nm}^{-1}$, which agrees well with experiment. A simulation snapshot of the dsRNA-TLR3 system near this corresponding optimal a spacing (such as for LL37-dsRNA) is shown in Figure S4. For interaction energies of $\epsilon = 4k_B T$ and $5k_B T$, the dependence of f_A on q is weaker, but activation is still maximized at a comparable inter-dsRNA spacing. Note that the optimal spacing observed here is slightly larger than that of the cognate TLR9 system, due to geometric differences in size between TLR3 and TLR9. Comparison to experiment (Figure 1E, 4C) indicates that an interaction energy of $\epsilon = 3k_B T$ is appropriate. The results also show that TLR3 binding and activation are more permissive for complexes with spacings that are sterically larger than the receptor than complexes with spacings that are smaller, in qualitative agreement with both the theoretical model and experiments.

The theoretical and simulation models address two limiting regimes of behavior: The former calculates TLR3 activation in a system where the total activation is limited by the number of available TLR3, whereas the latter assumes that the number of available TLR3 is large and the limiting constraint is the concentration of RNA-peptide complexes. The fact that we observe consistent behavior in these two limiting cases of TLR3 saturation and excess gives us confidence that we can address the basic aspects of the observed phenomenon with these simple models. Taken together, the dependence on the inter-dsRNA spacing, on the domain size and repeat number of dsRNA ordering, the residual ability of complexes with sterically larger dsRNA spacings to activate (especially with larger numbers of unit cells), and the inability of complexes with sterically smaller dsRNA spacings to activate, strongly suggest that the crystallinity of the dsRNA complex can structurally influence TLR3 activation significantly (Figure 5).

In summary, we demonstrate that the presentation of ordered lattices of dsRNA leads to amplification of TLR3 mediated IL-6 cytokine production in NEHKs. That it was recently shown that the presentation of ordered crystalline lattices of dsDNA leads to amplification of TLR9 mediated interferon- α secretion in plasmacytoid dendritic cells suggest that these may not be

unrelated phenomena (25). These results suggest a general picture in which immune signaling can be strongly influenced by AMP-immune ligand interactions. The resultant “ligand clustering” can in principle drive receptor clustering. The data here suggest that cationic proteins, peptides, or other cationic agents less than ~ 0.5 nm in size or much greater than ~ 3 nm in size do not significantly activate TLR3, since steric constraints will prevent the crystalline dsRNA rods from effectively recruiting TLR3. It is evident that immune modulation is complex and multifactorial. Quantitative differences in the degree of endosomal access between different types of dsRNA-peptide complexes can influence the level of TLR3 response in a manner independent of the nanocrystalline multivalent binding model. What is also equally clear is that not only can AMPs organize dsRNA into nanocrystalline structures recognizable by TLR3, the quantitative degree of immune activation is strongly influenced by crystalline parameters such as the inter-ligand spacing and the domain size of the ordering.

Materials and Methods

We characterized the structures of 15 polycation-dsRNA complexes at varying polycation-to-RNA charge ratios by using SAXS to extract the inter-RNA spacing and domain size. Induction of IL-6 production in human keratinocytes by these complexes was measured using ELISA. Crystallinity parameters were correlated with immune activation measurements using statistical bootstrapping techniques. dsRNA-containing complexes were co-localized to TLR3 using immunofluorescence staining. TLR3 involvement was confirmed with siRNA knockdown of TLR3 and RTqPCR of IL-6 transcription. A statistical mechanical model of TLR3 activation was developed and Monte-Carlo simulations of TLR3 binding to dsRNA complexes were conducted. Full materials and methods are found in the Supplementary Information.

Acknowledgments

E.Y.L. acknowledges support from the T32 Systems and Integrative Biology Training Grant at UCLA (T32GM008185) and the T32 Medical Scientist Training Program at UCLA (T32GM008042). R.L.G. acknowledges support from NIH R01AR064781, R01AI116576, and R01AI052453. G.C.L.W. acknowledges support from NIH 1R21AI122212. X-ray research was conducted at Stanford Synchrotron Radiation Lightsource, SLAC National Laboratory, supported by the US DOE Office of Basic Energy Sciences under Contract No. DE-AC02-76SF00515.

References

1. Uematsu S, Akira S (2008) Toll-Like receptors (TLRs) and their ligands. *Handb Exp Pharmacol* 183(183):1–20.
2. Alexopoulou L, Holt AC, Medzhitov R, Flavell RA (2001) Recognition of double-stranded RNA and activation of NF-kappaB by Toll-like receptor 3. *Nature* 413(6857):732–738.
3. Murphy K (2014) *Janeway's Immunobiology* (Garland Pub).
4. Herrath von MG, Bot A (2003) Immune responsiveness, tolerance and dsRNA: implications for traditional paradigms. *Trends in Immunology* 24(6):289–292.
5. Nelson AM, et al. (2015) dsRNA Released by Tissue Damage Activates TLR3 to Drive Skin Regeneration. *Cell Stem Cell* 17(2):139–151.
6. Zhang L-J, Gallo RL (2016) Antimicrobial peptides. *Curr Biol* 26(1):R14–9.
7. Miller LS (2008) Toll-like receptors in skin. *Adv Dermatol* 24:71–87.
8. Chen X, et al. (2013) Human antimicrobial peptide LL-37 modulates proinflammatory responses induced by cytokine milieu and double-stranded RNA in human keratinocytes. *Biochemical and Biophysical Research Communications* 433(4):532–537.
9. Grossman RM, et al. (1989) Interleukin-6 Is Expressed in High-Levels in Psoriatic Skin and Stimulates Proliferation of Cultured Human Keratinocytes. *PNAS* 86(16):6367–6371.
10. Goodman WA, et al. (2009) IL-6 signaling in psoriasis prevents immune suppression by regulatory T cells. 183(5):3170–3176.
11. Yang Y, et al. (2016) The RNA-binding protein Mex3B is a coreceptor of Toll-like receptor 3 in innate antiviral response. *Cell Res* 26(3):288–303.
12. Lai Y, et al. (2011) Viral double-strand RNA-binding proteins can enhance innate immune signaling by toll-like Receptor 3. *PLoS ONE* 6(10):e25837.
13. Ganguly D, et al. (2009) Self-RNA-antimicrobial peptide complexes activate human dendritic cells through TLR7 and TLR8. *J Exp Med* 206(9):1983–1994.
14. Endoh T, Ohtsuki T (2009) Cellular siRNA delivery using cell-penetrating peptides modified for endosomal escape. *Advanced Drug Delivery Reviews* 61(9):704–709.
15. Nathan F Boussein, Christopher S McAllister, Kai K Ewert, Charles E Samuel A, Cyrus R Safinya (2007) Structure and Gene Silencing Activities of Monovalent and Pentavalent Cationic Lipid Vectors Complexed with siRNA[†]. *Biochemistry* 46(16):4785–4792.

16. Singha K, Namgung R, Kim WJ (2011) Polymers in small-interfering RNA delivery. *Nucleic Acid Ther* 21(3):133–147.
17. Wong GCL, Pollack L (2010) Electrostatics of strongly charged biological polymers: ion-mediated interactions and self-organization in nucleic acids and proteins. *Annu Rev Phys Chem* 61:171–189.
18. Pollack L (2011) SAXS Studies of Ion–Nucleic Acid Interactions. *Annu Rev Biophys* 40(1):225–242.
19. Livolant F, Leforestier A (1996) Condensed phases of DNA: Structures and phase transitions. *Progress in Polymer Science* 21(6):1115–1164.
20. Sanders LK, et al. (2007) Control of electrostatic interactions between F-actin and genetically modified lysozyme in aqueous media. *Proc Natl Acad Sci USA* 104(41):15994–15999.
21. DeRouchey J, Netz RR, Radler JO (2005) Structural investigations of DNA-polycation complexes. *Eur Phys J E* 16(1):17–28.
22. Evans HM, et al. (2003) Structural polymorphism of DNA-dendrimer complexes. *Phys Rev Lett* 91(7):075501.
23. Rau DC, Parsegian VA (1992) Direct measurement of the intermolecular forces between counterion-condensed DNA double helices. Evidence for long range attractive hydration forces. *Biophysj* 61(1):246–259.
24. Gilliet M, Lande R (2008) Antimicrobial peptides and self-DNA in autoimmune skin inflammation. 20(4):401–407.
25. Schmidt NW, et al. (2015) Liquid-crystalline ordering of antimicrobial peptide-DNA complexes controls TLR9 activation. *Nat Mater* 14(7):696–700.
26. Liu L, et al. (2008) Structural basis of toll-like receptor 3 signaling with double-stranded RNA. *Science* 320(5874):379–381.
27. Lai Y, et al. (2011) LL37 and Cationic Peptides Enhance TLR3 Signaling by Viral Double-stranded RNAs. *PLoS ONE* 6(10):e26632.
28. Radler JO, Koltover I, Salditt T, Safinya CR (1997) Structure of DNA-cationic liposome complexes: DNA intercalation in multilamellar membranes in distinct interhelical packing regimes. *Science* 275(5301):810–814.
29. Mishra A, Gordon VD, Yang L, Coridan R, Wong GCL (2008) HIV TAT Forms Pores in Membranes by Inducing Saddle-Splay Curvature: Potential Role of Bidentate Hydrogen Bonding. *Angew Chem Int Ed* 47(16):2986–2989.

30. Brooks H, Lebleu B, Vivès E (2005) Tat peptide-mediated cellular delivery: back to basics. *Advanced Drug Delivery Reviews* 57(4):559–577.
31. Park CB, Kim HS, Kim SC (1998) Mechanism of Action of the Antimicrobial Peptide Buforin II: Buforin II Kills Microorganisms by Penetrating the Cell Membrane and Inhibiting Cellular Functions. *Biochemical and Biophysical Research Communications* 244(1):253–257.
32. Park CB, Yi KS, Matsuzaki K, Kim MS, Kim SC (2000) Structure-activity analysis of buforin II, a histone H2A-derived antimicrobial peptide: the proline hinge is responsible for the cell-penetrating ability of buforin II. *PNAS* 97(15):8245–8250.
33. Feuerstein BG, Williams LD, Basu HS, Marton LJ (1991) Implications and concepts of polyamine-nucleic acid interactions. *J Cell Biochem* 46(1):37–47.
34. Tabor CW, Tabor H (1984) Polyamines. *Annu Rev Biochem*.
35. Moinard C, Cynober L, de Bandt J (2005) Polyamines: metabolism and implications in human diseases. *Clinical Nutrition* 24(2):184–197.
36. Lande R, et al. (2014) The antimicrobial peptide LL37 is a T-cell autoantigen in psoriasis. *Nat Commun* 5:5621.
37. Morizane S, Gallo RL (2012) Antimicrobial peptides in the pathogenesis of psoriasis. *J Dermatol* 39(3):225–230.
38. Lande R, et al. (2015) Cationic antimicrobial peptides in psoriatic skin cooperate to break innate tolerance to self-DNA. *Eur J Immunol* 45(1):203–213.
39. Ohto U, et al. (2015) Structural basis of CpG and inhibitory DNA recognition by Toll-like receptor 9. *Nature* 520(7549):702–705.
40. Dubacheva GV, Curk T, Auzély-Velty R, Frenkel D, Richter RP (2015) Designing multivalent probes for tunable superselective targeting. *Proc Natl Acad Sci USA* 112(18):5579–5584.
41. Dubacheva GV, et al. (2014) Superselective Targeting Using Multivalent Polymers. *J Am Chem Soc* 136(5):1722–1725.

Figure Legends

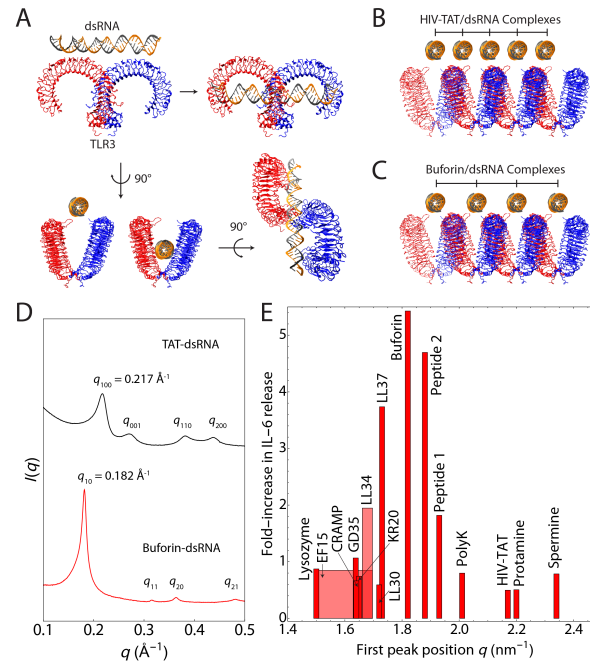


Figure 1: IL-6 production in keratinocytes through TLR3 activation depends on the inter-dsRNA spacing within self-assembled polycation-dsRNA electrostatic complexes. (A) Illustration of dsRNA binding to TLR3 from two orthogonal views based on the known crystal structure of mouse TLR3 (PDB ID: 3CIY (26)). (B) Smaller geometric spacings between ordered dsRNA columns (such as in HIV-TAT/dsRNA complexes) reduce TLR3 activation because they sterically hinder accessibility of dsRNA to the receptors. (C) In contrast, larger geometric spacings between ordered dsRNA columns (such as in buforin-dsRNA complex) optimize electrostatic interactions with TLR3, leading to binding of multiple TLR3s simultaneously and amplification of the immune response. (D) Representative SAXS data from peptide-dsRNA complexes that induce strong IL-6 production (buforin-dsRNA, red), and complexes that do not (TAT-dsRNA, black). The TAT-dsRNA complex forms a 3D hexagonal lattice with a first peak position at $q_{100} = 0.217 \text{ \AA}^{-1}$ and an approximate inter-dsRNA spacing of $a \sim 2.90 \text{ nm}$. The buforin-dsRNA complex forms a 2D hexagonal lattice with a first peak position at $q_{10} = 0.182 \text{ \AA}^{-1}$ and an inter-dsRNA spacing of $a \sim 3.45 \text{ nm}$. All higher order reflections are labeled. (E) Normalized fold-increase in IL-6 production by NHEK induced by polycation-dsRNA complexes. The immune response correlates strongly with the SAXS measurements of their first diffraction peak positions, which are inversely proportional to the inter-dsRNA spacing. The distance correlation test for statistical independence is $R_{\text{dCor}} = 0.371$ [0.327, 0.492] (95% CI) with $P = 0.022$ (Figure S1A). The MIC nonlinear correlation was $\text{MIC} = 0.652$ [0.414, 0.894] with $P < 10^{-5}$ (Figure S1B). Inter-dsRNA spacings corresponding to first peak positions $q \sim 1.7\text{--}1.9 \text{ nm}^{-1}$ result in amplified IL-6 production. Wide bars with shading indicate a range of first peak positions for two of the polycation-dsRNA complexes (EF15, LL34) based on SAXS measurements (see SI discussion). Narrow bars indicate no significant observable change in first peak positions across stoichiometric ratios.

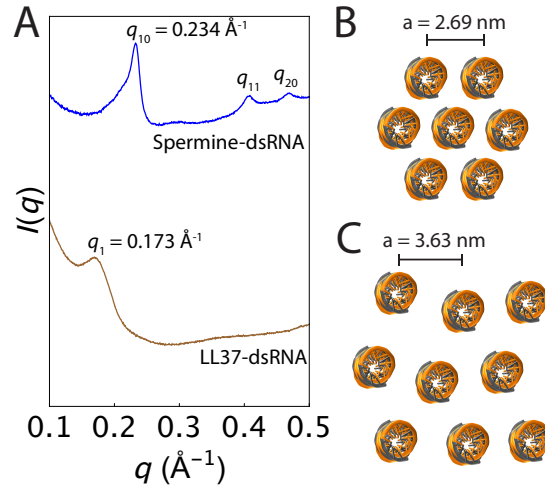


Figure 2: Differences in structure of polycation-dsRNA complexes predict their abilities to amplify cytokine production. Ordered dsRNA columnar complexes have diverse structures with varying inter-dsRNA spacings. The presentation of “open” dsRNA complexes with spacings commensurate with the steric size of TLR3 ($a = 3.3\text{-}3.7 \text{ nm}$) highly amplify IL-6 production in NHEK, while “closed” dsRNA complexes with spacings smaller than the steric size of TLR3 ($d < 3.2 \text{ nm}$) result in reduced TLR3 activation and IL-6 production. (A) Representative SAXS data of spermine and LL37-dsRNA complexes. LL37-dsRNA complexes induce $\sim 5\times$ the IL-6 production from NHEK compared to spermine-dsRNA complexes. Spermine-dsRNA complexes (blue) form a 2D hexagonal columnar phase with a first peak position at $q_{10} = 0.234 \text{ \AA}^{-1}$, corresponding to an inter-dsRNA spacing of $a = 2.69 \text{ nm}$ (B). All higher order reflections of the spermine-dsRNA complex are labeled with their Miller indices. In comparison, the LL37-dsRNA complexes (brown) form a disordered columnar phase with a first peak position at $q_1 = 0.173 \text{ \AA}^{-1}$ and an average inter-dsRNA spacing of $a = 3.63 \text{ nm}$ (C). This difference in inter-dsRNA spacing drastically changes the ability of the complex to activate TLR3, as observed in Figure 1E.

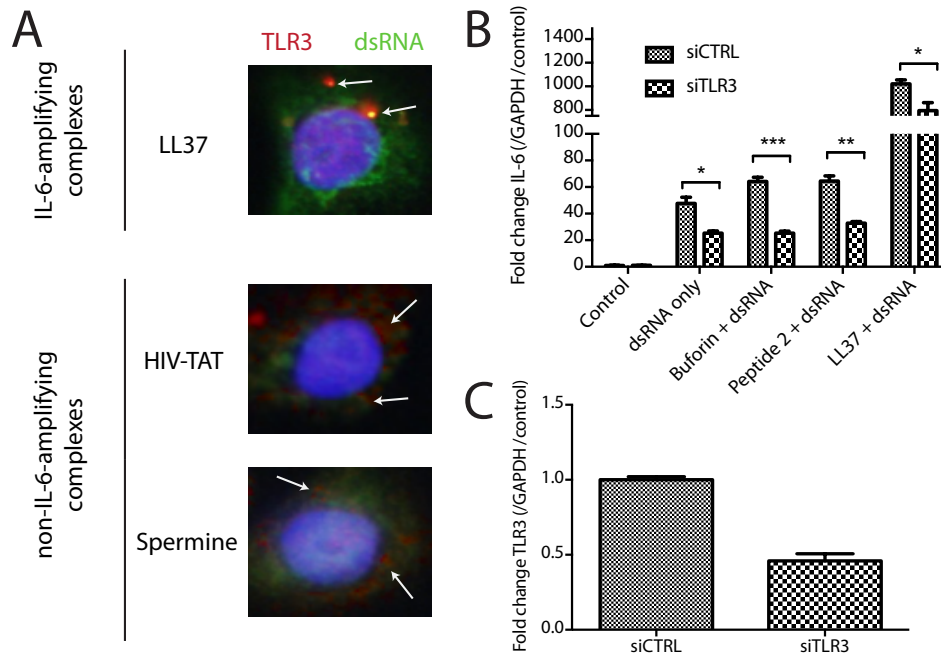


Figure 3: Cytokine-inducing polycation-dsRNA complexes activate NHEK via TLR3. NHEK were stimulated for 4 hrs with biotinylated poly(I:C) complexed with either IL-6-amplifying LL37 or non-IL-6-amplifying HIV-TAT and spermine. Cells were fixed in 4% PFA for 10 mins, and then incubated with rabbit anti-TLR3. After washing, AlexaFluor 488-labelled streptavidin was used to visualize poly(I:C), and 576-labeled anti-rabbit secondary antibody was used to visualize TLR3. Cell nuclei were stained with DAPI. Cells were imaged using an Olympus BX41 microscope. (A) We observe strong co-localization between TLR3 (red) and polycation-dsRNA complexes (green) within NHEK (white arrows indicate overlap). Both IL-6-amplifying and non-IL-6-amplifying polycation-dsRNA complexes co-localize with TLR3, indicating that endosomal access is a necessary but not sufficient criterion for high levels of cytokine production. (B) RTqPCR of IL-6 transcripts during siRNA knockdown of TLR3 confirms that TLR3 activation by strongly-activating polycation-dsRNA complexes are predominantly responsible for IL-6 production. The buforin-poly(I:C), Peptide 2-Poly(I:C), and LL37-poly(I:C) complexes all demonstrate statistically significant reduction in IL-6 production in the presence of siTLR3 compared to control siRNA ($p^* < 0.05$ for dsRNA only, $p^{***} < 0.001$ for buforin-dsRNA, $p^{**} < 0.01$ for Peptide 2-dsRNA, $p^* < 0.05$ for LL37-dsRNA). Data is shown relative to expression of the GAPDH housekeeping gene. (C) Data showing successful knockdown of TLR3 in NHEK using siTLR3 ($p < 0.001$). Pairwise two-tailed t-tests were used to analyze siRNA knockdowns in both (B) and (C) (Error bars show mean \pm SEM, $n = 3$).

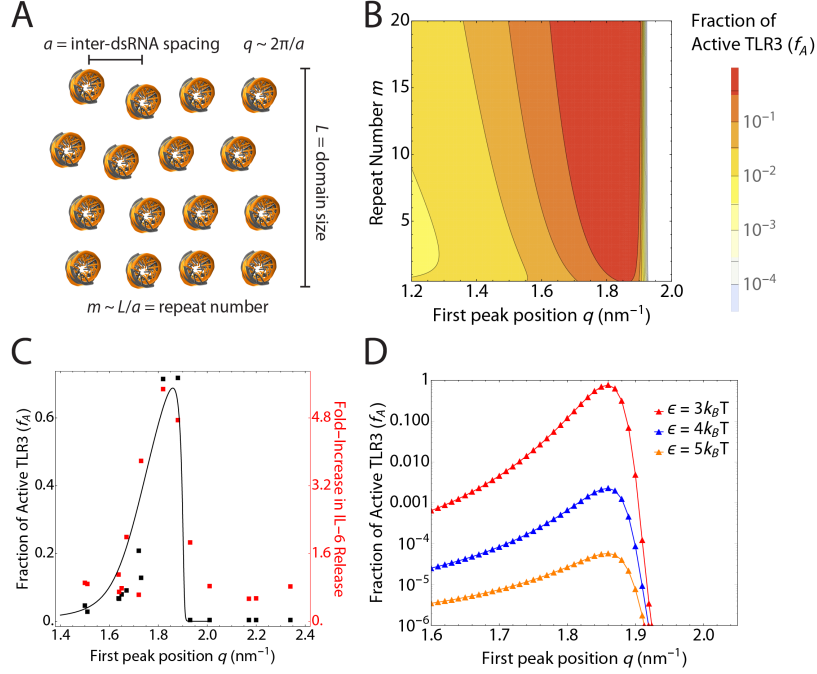


Figure 4: Coarse-grained model of TLR3 binding to RNA bundles exhibits dependence on inter-dsRNA spacing and repeat number in agreement with experimental observations. (A) Schematic depicting the crystallinity parameters of an example peptide-dsRNA complex. The inter-dsRNA spacing, first peak position, domain size, and repeat number are defined. (B) Contour plot of the fraction of active TLR3 receptors f_A as a function of the repeat number m (e.g. number of dsRNA rods per cluster) and the first peak position q , which is inversely proportional to the inter-dsRNA spacing ($a = 2\pi/q$). For this snapshot, the prefactor was chosen as $C^* = l \frac{C_{RNA}}{\rho_{TLR}} = 10^{-2}$, with $B = 30k_B T$ and interaction energy $\epsilon^* = 2k_B T$. The TLR3-RNA interaction model takes into account the steric size of TLR3 ($\sigma = 4.4nm$), which is wider than TLR9 due to a larger opening angle. High levels of TLR3 binding and TLR3 activation are denoted in orange, and low levels of binding and TLR3 activation are denoted in yellow to blue. We observe that maximal activation occurs at inter-dsRNA spacings corresponding to first-peak positions $q = 2\pi/a$ between $q \sim 1.7$ - 1.9 nm^{-1} (~ 3.3 - 3.7 nm), but that this region expands as repeat number increases. Inter-dsRNA spacings that are much smaller than the steric size of TLR3 do not lead to increased activation ($q > 2.0 \text{ nm}^{-1}$) due to steric repulsion between adjacent receptors and dsRNA rods. (C) To compare the theoretical prediction of TLR3 activation to the experimental data for the 15 characterized complexes, we calculate the fraction of active TLR3 f_A using the parameters q and m from Table S1 and SI Eqn 3. We find good quantitative agreement between the theoretical prediction of active TLR3 (left vertical axis, black) and measured IL-6 production from NHEK (right vertical axis, red) for experimentally measured q and m (Figure 1E). The vertical axes are rescaled for consistency. To guide the eye, the black line denotes the theoretical curve from SI Eqn. 3 calculated for $m = 6$. (D) Grand canonical Monte Carlo simulations of TLR3 binding to crystalline lattices of dsRNA recapitulate features observed in the theoretical model and experimental data. The fraction of active TLR3 receptors (f_A) is plotted against the first peak position q at $B = 30k_B T$ and $m = 4$ for interaction energies $\epsilon = 3k_B T$, $4k_B T$, and $5k_B T$.

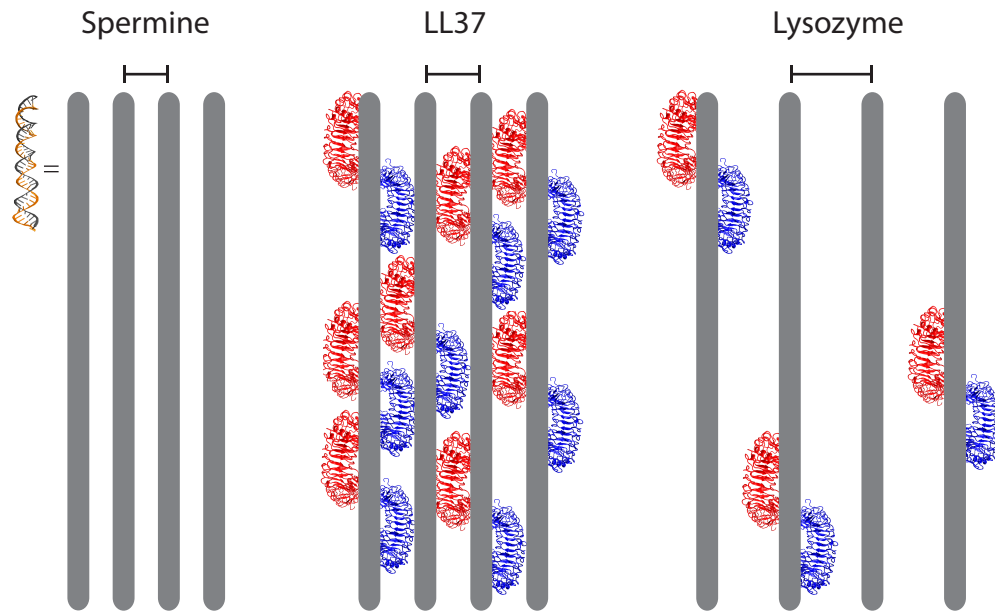


Figure 5: **Superselective binding of TLR3 to polycation-dsRNA complexes occurs only at inter-dsRNA spacings commensurate with the steric size of TLR3.** This schematic demonstrates the drastic differences in TLR3 binding and activation as the inter-dsRNA spacing is varied from “close-packed” to “open”. This is a top-down view of mobile TLR3 receptors (red and blue) in the endosomal membrane binding to clustered dsRNA ligands (gray). Spermine-dsRNA complexes with tightly packed dsRNA rods does not allow for steric access of TLR3 paddles between rods. LL37-dsRNA complexes have optimal inter-dsRNA spacings well-matched to the width of the TLR3 paddles, which drives TLR3 receptor recruitment and clustering and drastically amplifies immune activation. “Wide-packed” lysozyme-dsRNA complexes can accommodate TLR3 binding and activation, but loss of multivalency between adjacent dsRNA rods due to reduced backbone interactions leads to a lower density of TLR3 binding.

Supplementary Information

Crystallinity of dsRNA-AMP complexes modulates TLR3-mediated inflammation

Ernest Y. Lee¹, Toshiya Takahashi², Tine Curk^{3,4}, Jure Dobnikar^{3,4,5*}, Richard L. Gallo^{2*}, Gerard C. L. Wong^{1*}

¹ Department of Bioengineering, University of California, Los Angeles, Los Angeles, CA 90095, United States

² Department of Dermatology, University of California, San Diego, La Jolla, CA 92093, United States

³ Department of Chemistry, University of Cambridge, Cambridge, UK

⁴ Beijing National Laboratory for Condensed Matter Physics & CAS Key Laboratory of Soft Matter Physics, Institute of Physics, Chinese Academy of Sciences, Beijing 100190, China

⁵ School of Physical Sciences, University of Chinese Academy of Sciences, Beijing 100049, China

*To whom correspondence should be addressed:

Gerard C.L. Wong

Department of Bioengineering, University of California, Los Angeles, 4121 Engineering V UCLA
Los Angeles, CA 90095. Tel: (310) 794-7684 Email: gclwong@seas.ucla.edu

Richard L. Gallo

Department of Dermatology, University of California, San Diego, 3350 La Jolla Village Drive, San Diego, CA 92161. E-mail address: rgallo@ucsd.edu

Jure Dobnikar

Department of Chemistry, University of Cambridge, Cambridge, UK

Email address: jd489@cam.ac.uk

1. Supplementary Tables

Table S1: Data from SAXS studies and cell experiments for dsRNA complexed with various polycationic molecules. We report crystallinity parameters of the structurally-characterized polycation-dsRNA complexes, including the first peak position q , the inter-RNA spacing ($a = 2\pi/q$), the domain size L , the number of repeats m , the measured structure, and the mean normalized fold-increase in IL-6 production from keratinocytes relative to baseline production.

Peptide	Mean Normalized Fold Increase in IL-6 Release	First Peak Position q (nm^{-1})	Inter-RNA Spacing a (nm)	Domain Size L (nm)	Number of Repeats m	Phase
LL37	3.74	1.73	3.63	2.11	0.58	Disordered columnar
Buforin	5.43	1.82	3.45	39.36	11.40	Hexagonal
Peptide 1	1.82	1.93	3.26	13.67	4.20	Disordered columnar
Peptide 2	4.70	1.88	3.34	36.40	10.89	Hexagonal
GD35	1.07	1.64	3.84	4.92	1.28	Disordered columnar
LL34	1.95	1.67 – 1.70	3.69-3.76	4.59	1.22	Square
KR20	0.75	1.66	3.79	5.50	1.45	Square
EF15	0.85	1.51 – 1.70	3.69-4.16	5.93	1.42	Disordered columnar
LL30	0.59	1.72	3.65	8.30	2.27	Square
Lysozyme	0.87	1.50	4.19	31.17	7.44	Hexagonal
Spermine	0.79	2.34	2.69	17.80	6.63	Hexagonal
Protamine	0.51	2.20	2.86	13.46	4.71	Hexagonal
PolyK	0.80	2.01	3.13	15.98	5.11	Hexagonal
HIV-TAT	0.50	2.17	2.90	17.18	5.93	Hexagonal
CRAMP	0.66	1.64	3.83	4.37	1.14	Disordered columnar

Table S2. List of primers used for RT-qPCR: Gene symbols and forward and reverse primer sequences for each gene are shown in the table below.

Gene	Strand	Primer sequence
GAPDH	Forward	TGGGCTACACTGAGCACCAG
	Reverse	GGGTGTCGCTGTTGAAGTCA
IL-6	Forward	AATTCGGTACATCCTCGACGG
	Reverse	TTGGAAGGTTTCAGGTTGTTTCT

2. Experimental Methods

2.1 Preparation of self-assembled polycation-dsRNA complexes

Lyophilized cationic peptides LL37 (LLGDFFRKSKEKIGKEFKRIVQRIKDFLRNLPRTES), buforin (TRSSRAGLQFPVGRVHRLLRK), CRAMP (GLLRKGGEKIGEKLLKIGQKIKNFFQKLVPQPEQ), and HIV-TAT (47-57, YGRKKRRQRRR) were purchased from Anaspec or Genemed Synthesis Inc. ($\geq 95\%$ purity by HPLC). The following cationic peptides were also custom synthesized (LifeTein, $\geq 95\%$ purity by HPLC): GD35 (GDFFRKSKEKIGKEFKRIVQRIKDFLRNLPRTES), LL34 (LLGDFFRKSKEKIGKEFKRIVQRIKDFLRNLPVPR), LL30 (LLGDFFRKSKEKIGKEFKRIVQRIKDFLRN), KR20 (KRIVQRIKDFLRNLPRTES), EF15 (EFKRIVQRIKDFLRN), Peptide 1, and Peptide 2. Other polycationic agents used include human lysozyme, polylysine (MW $\sim 70,000$), spermine, and protamine sulfate (Sigma Aldrich). All cationic agents were dissolved in nuclease-free water (Ambion) to 10 mg/mL. For SAXS and cell experiments, poly(I:C) (high molecular weight) and poly(A:U) (Invivogen) were directly resuspended in physiological buffer (100 mM NaCl + 10 mM HEPES, pH 7.4) to 5 mg/mL. Polycation-dsRNA complexes were formed by incubating the peptide with dsRNA (1-5 mg/mL for SAXS experiments, 10-20 $\mu\text{g/mL}$ for cell experiments) at specific peptide-to-RNA charge ratios ($P/\text{RNA} = 1/4, 1/2, 1/1, 2/1, 4/1$). For a specific cationic reagent, the same charge ratios were used in both SAXS and cell experiments.

2.2 SAXS Experiments and Data Analysis

We mapped out the structural phase diagrams of peptide-dsRNA complexes by incubating peptides (10 mg/mL) with dsRNA (5 mg/mL) at specific charge ratios in microcentrifuge tubes as described above. After thorough mixing and centrifugation, precipitated complexes are hermetically sealed in 1.5 mm quartz capillaries (Hilgenberg GmbH, Mark-tubes). SAXS experiments were performed at Stanford Synchrotron Radiation Lightsource (SSRL, Beamline 4-2) using monochromatic X-rays with an energy of 9 keV. A Rayonix MX225-HE detector (pixel size 73.2 μm) was used to measure the scattered radiation. Independent identical samples were prepared and measured over multiple timepoints to ensure consistency. 2D powder diffraction patterns were integrated using the Nika 1.74 (1) package for Igor Pro 6.37 and FIT2D (2). SAXS data were analyzed by plotting integrated scattering intensity against the momentum transfer q using Mathematica. Peak positions were measured by fitting diffraction peaks to a Lorentzian. Structures of complexes were solved by calculating ratios between the q -positions of all measured peaks and comparing them with the permitted reflections for known liquid-crystalline phases. The lattice parameter(s) of each phase were calculated by linear regression through points corresponding to measured and theoretical peaks. The lattice parameter a indicates the inter-dsRNA spacing between RNA columns. For each complex, the inter-dsRNA spacing a is estimated from the first peak position by the formula $a = 2\pi/q_1$.

To determine the phase and lattice parameters for each nanocrystalline complex, we measure the q peak positions and relate them to the Miller indices for powdered averaged

phases. $q_{hk} = \frac{2\pi}{a}\sqrt{h^2 + k^2}$ for square columnar lattices, $q_{hk} = \frac{2\pi}{a}\sqrt{\frac{4}{3}(h^2 + k^2 + hk)}$ for hexagonal columnar lattices, and $q_1 = \frac{2\pi}{a}$ for disordered columnar lattices. Square and hexagonal lattices were assigned based on fitting the measured q positions to the above equations. Typical square lattices will have reflections at q_{10} and q_{11} with a ratio of 1: $\sqrt{2}$. In contrast, typical hexagonal lattices will have reflections at q_{10} , q_{11} , and q_{20} with a ratio of 1: $\sqrt{3}$:2. Procedures to assign these liquid-crystalline phases are similar to those found here (3).

In addition to quantifying the lattice parameters and inter-dsRNA spacings in each complex, we also measured average domain size L of each complex. From that value, we extracted the number of repeat units m in each complex. To obtain the domain size, we approximated the structure factor peaks as squared-Lorentzians. Comparing Gaussian and squared-Lorentzian lineshapes, the Lorentzian lineshape yielded the best fit for all of the complexes. The form of the equation used for the fit was

$$S(q) = \frac{w^3}{4\pi \left(|q - q_0|^2 + \left(\frac{w}{2}\right)^2 \right)^2}$$

where q_0 is the location of the peak and w is the peak width (4). The experimental SAXS data was background subtracted, and the first peak for each complex was fitted using non-linear least square regression in Mathematica. The extracted value for peak width w can be related to the average linear domain size L using Warren's approximation (5). For the squared-Lorentzian lineshape, the domain size is related to w via the equation (6).

$$L = \frac{(8\pi)^{\frac{1}{2}}}{\frac{w}{2}}$$

We assume that a typical bundle has an area proportional to L^2 . To calculate the number of repeat units in each complex m , we estimated this by dividing the linear domain size L by the measured inter-dsRNA spacings a ($m = L/a$). The resulting values for L and m for each liquid-crystalline complex are reported in Table S1.

2.3 Reverse transcription-quantitative PCR (RTqPCR) analyses

Control siRNA and TLR3 siRNA were purchased from Dharmacon. During each keratinocyte stimulation, 5 nM of each siRNA was electroporated into NHEKs as described previously (7). Total cellular RNA was extracted using the PureLink RNA isolation kit and RNA was reverse transcribed to cDNA using iScript cDNA synthesis kit (Bio-rad). Quantitative, real-time PCR was performed on the CFX96 real time system (Biorad) using TaqMan® Gene Expression Master Mix. The expression of GAPDH gene was used as a house keeping gene to normalize data in human cells. Specific primer sequences are shown in Table S2 in the Supplementary Information.

2.4 Keratinocyte Stimulation Experiments

Primary neonatal human epidermal keratinocytes (NHEKs) were purchased from Invitrogen. NHEKs were grown in serum free EpiLife medium supplemented with 0.06 mM

CaCl₂, EpiLife Defined growth supplements (EDGS) (Invitrogen) and antibiotics, and passage 4-6 cells were used for experiment. Cells at 60%-80% confluence were starved overnight without EDGS prior to treatment. NHEKs were treated with polycationic agent/peptide (10 ug/mL) or vehicle control mixed with poly(I:C) (0.3 ug/mL) for 6 hrs (RTqPCR) and 18 hrs (ELISA). IL-6 protein volume using supernatant for NHEKs after indicated stimulation were measured by human IL-6 ELISA kit (R&D systems, Minneapolis, MN) per manufacturer's protocol. All stimulation experiments were done in triplicate. IL-6 release for each polycation-dsRNA complex was normalized relative to control stimulation and reported in Table S1.

2.5 NHEK Immunofluorostaining Experiments

NHEKs were grown on 8-well chamber slides (Thermo Fisher Scientific, Waltham, MA, USA). NHEKs were stimulated with biotinylated poly(I:C) (Invivogen, San Diego, CA, USA) with LL37 (Genemed Synthesis), HIV-TAT, or Spermine for 4 hr. Then NHEK were fixed in 4% PFA for 10 mins prior to immunofluorescence staining. Fixed and permeabilized cells were incubated with anti-TLR3 antibody (ab137722, abcam, Cambridge, MA, USA) followed by streptavidin-conjugated AlexaFluor 488 (Thermo Fisher Scientific) and 576-coupled anti-rabbit secondary antibody (Thermo Fisher Scientific). Nuclei were counterstained with DAPI. All images were taken with an Olympus BX41 microscope.

2.6 Statistical Analyses

Bootstrapping calculations to compute confidence intervals and P-values were done using the distance correlation function in the 'energy' package in R. MIC bootstrapping calculations were done using the 'minerva' package in R. We tested the relationship between the inter-dsRNA spacing and cytokine production by conducting a null hypothesis significance test with a significance level of $\alpha = 0.05$. Analysis of RTqPCR siRNA knockdown data was done in Mathematica.

3. Theoretical Model and Methods

The model builds on the TLR9 – DNA-peptide interaction model (4) generalized to take into account the limited number of TLR3 receptors in the endosomal membrane. Furthermore, the effect of varying nanocrystalline cluster sizes between different peptide – RNA complexes is explicitly considered.

We use a Langmuir-like approach and assume that there are k possible binding sites for TLR receptors on each RNA cluster (i.e. k is the maximum number of TLR receptors that can bind to each peptide-RNA cluster), all binding sites are identical and independent. The number k will be determined by the cluster size (i.e. the repeat number m) and the individual RNA length. We assume that clusters have a cuboidal shape, all RNA rods in the cluster are aligned parallel and only one face of a presenting a RNA-grill to the membrane interacts with membrane bound TLR3. Therefore, the number of possible bound TLR is: $= k_0 m$, where m is the repeat number and k_0 denotes an effective number of TLR that can bind along a single RNA rod. The TLR3 receptor molecules do not interact with each other, except for the hard-core excluded volume interaction forbidding their overlaps.

3.1 Analytical Theory Derivation

The partition function counting all possible bound/unbound states of a RNA-peptide cluster lying on a TLR3 decorated membrane is

$$Q = \left(1 + (1 - f_A)e^{-\varepsilon/k_B T}\right)^k \quad (1)$$

where ε is the binding free energy including the chemical potential μ of the TLR3 on the endosomal membrane: $\varepsilon = \Delta G + \mu$, with ΔG the Gibbs free energy of binding of a single TLR3 to a RNA-peptide binding site. The number of available (unbound) receptors on the membrane is $N^{tot}(1 - f_A)$ where $f_A = \frac{N_A}{N^{tot}}$ is the fraction of bound (activated) receptors with N_A and N^{tot} the number of activated (bound) and total number of receptors, respectively. The binding free energy for the first bond is $\varepsilon = \Delta G - k_B T \log(N^{tot} / A\rho_0)$ with ρ_0 the reference density and $k_B T$ the thermal energy. Subsequent bonds are weaker: $\varepsilon^* = \varepsilon - k_B T \log(1 - f_A)$

due to the depletion of available receptors. The average number of bound TLR per RNA-peptide cluster is given by the Langmuir adsorption isotherm $n_b = k \frac{(1 - f_A)e^{-\varepsilon/k_B T}}{1 + (1 - f_A)e^{-\varepsilon/k_B T}}$. Furthermore, the

mean number of bound clusters is determined in terms of the membrane coverage: $\Theta = \frac{zQ}{1 + zQ}$

, i.e. the surface density of clusters. z is the dimensionless activity, i.e. the probability that an unbound cluster is found on a membrane within area a_k that a single cluster occupies.

The total number of bound clusters: $N = \Theta \frac{A}{a_k}$ is proportional to the membrane coverage, but depends also on the (unknown) size of the membrane A and the cluster excluded area a_k . Larger clusters occupy more space on the membrane, therefore $a_k = ka_1$, with a_1 a constant specifying the space occupied per single TLR binding site, a_1 is approximately of the size of a single TLR3 receptor.

It is not possible at present to measure the full size distribution of all the endosomal compartments in keratinocytes used in our experiments; therefore, we cannot predict the absolute number of bound TLR3. However, we can calculate the number of bound TLR3 up to proportionality constant. Finally, we can obtain the average number of all active receptors by multiplying the number of clusters with the average number of bound TLR per cluster:

$$N_A = n_b N = n_b \Theta \frac{A}{a_1 k}$$

Dividing by the total number of receptors and expanding we get

$$f_A = \frac{zA}{N^{tot} a_1} \frac{(1 - f_A)e^{-\varepsilon/k_B T} \left(1 + (1 - f_A)e^{-\varepsilon/k_B T}\right)^{k-1}}{1 + z \left(1 + (1 - f_A)e^{-\varepsilon/k_B T}\right)^k} \quad (2)$$

which needs to be solved self consistently for the fraction of bound (activated) receptors f_A . This theory is similar to the one we previously presented for the binding of the DNA-peptide complexes to TLR9 (4). However, we now consider the number of TLR3 receptors to be limited,

while previously, we have considered TLR9 to be in excess compared to DNA-peptide clusters ($f_A \ll 1$). We expect that the present theory more accurately models the realistic system where the number of TLR3 in endosomal compartments is limited. However, we stress that both approaches give qualitatively similar results, and that both approaches can explain the experimental observations.

Since we expect the number of TLR3 receptors to be the limiting factor in RNA-peptide cluster adsorption, rather than the total coverage of the membrane with clusters, $zQ \ll 1$ and Eq. (2) can be well approximated with $f_A = \frac{zA}{N^{tot}a_1} (1 - f_A) e^{-\varepsilon/k_B T} (1 + (1 - f_A) e^{-\varepsilon/k_B T})^{k-1}$.

The dimensionless activity z is the probability that an unbound cluster is found on a membrane within lattice size a_k , hence we estimate it is: $z = l a_k c_{clust}$, where l is the length scale in our system – the interaction range (height of a single TLR $\sim 1\text{nm}$) and c_{clust} is the concentration of clusters in solution. In experiments the RNA strand concentration c_{RNA} and molar ratios to peptides was kept fixed. Therefore, the density of clusters will be inversely proportional to the number of RNA strands per cluster m^2 : $c_{clust} = \frac{c_{RNA}}{m^2}$. We remember that the number of possible TLR3 attachment sites is also determined by the repeat number: $k = k_0 m$. Using these relations, we can compute the fraction of activated TLR3 as a function of the repeat number m and interaction energy ε :

$$f_A = C \frac{k_0}{m} (1 - f_A) e^{-\frac{\varepsilon}{k_B T}} \left(1 + (1 - f_A) e^{-\frac{\varepsilon}{k_B T}} \right)^{k_0 m - 1} \quad (3)$$

The prefactor $C = l \frac{c_{RNA}}{\rho_{TLR}}$ depends on the ratio between the densities of RNA in solution and TLR3 on the membrane. Experimental were performed at $c_{RNA} = 5 \text{ g/L}$ with the average RNA molecular weight: $M_{RNA} = 408\text{kDa}$. We do not know the absolute density of TLR3 receptors in endosomal compartments, however, a reasonable value would be about one TLR3 per 100 square nanometers: $\rho_{TLR} \approx \frac{1}{100\text{nm}^2}$. The length scale (TLR3 – RNA interaction range) is about a nanometer, $l \approx 1\text{nm}$. Therefore, the prefactor can be estimated as: $C \approx 10^{-3}$. The effective number of TLR3 that can bind along a single RNA rod depends on the RNA length that is presented to the membrane, we assume it to be one persistence length ($l_p^{RNA} \approx 50\text{nm}$). The TLR3 horseshoe size is $\sigma = 4.4\text{nm}$; TLR3 is a dimer made from two horseshoes (or “paddles”), see Figure S4. Therefore, $k_0 \approx \frac{l_p^{RNA}}{2\sigma} \approx 5$.

Following Ref. (4) the TLR3 – dsRNA interaction has two contributions

$$\varepsilon(a) = \varepsilon^* + 2U(a) \quad (4)$$

The main part, ε^* , is the cognate binding of RNA to the TLR dimer. However, there is also a weak nonspecific contribution due to electrostatics between an RNA and an adjacent TLR3 paddle: $U(a)$, which depends on a , the RNA spacing within the cluster. The factor 2 reflects that TLR3 is

a dimer of two “paddles” (see Figures 1 and 5 in the main text). This contribution is only present when the RNA is organized into clusters

$$U(a) = -B \frac{e^{-\kappa(a-\sigma/3)}}{a-\sigma/3} + \left(\frac{\sigma}{12(a-2\sigma/3)} \right)^{12} k_B T, \quad (5)$$

where the first term captures the electrostatic attraction and the second term the steric repulsion between a TLR3 paddle and an adjacent RNA strands in a cluster. $\sigma_{TLR3} = 4.4 \text{ nm}$ is the TLR3 size which is slightly larger than the TLR9 size $\sigma_{TLR9} = 4.0 \text{ nm}$ (4). The Debye screening length is $\kappa^{-1} = 0.8 \text{ nm}$ at physiological salt concentration. The prefactor B defines the strength of electrostatic interaction, a value $B = 30 k_B T \text{ nm}$ is adopted from TLR9 (4).

Inserting Eqs. (4,5) into Eq. (3) we obtain the fraction of activated receptors as a function of the cluster spacing expressed with the lattice vector $q = \frac{2\pi}{a}$, and the unit cell repeat number m : $f_A = f_A(q, m)$.

3.2 Simulation Model

Grand canonical Monte Carlo simulations were performed by simulating an array of RNA chains lying flat on a membrane as shown in Figure S4. We simulate a single persistence length of dsRNA $\sim 50 \text{ nm}$. On length scales larger than persistence length, the cluster is likely more orientationally disordered. The membrane acts as a reservoir for TLR3. TLR3 can bind to DNA with binding energy $\varepsilon^*(a)$ which includes the chemical potential of TLR3 μ_{TLR} . Receptor depletion is not considered in MC simulations and μ_{TLR} is treated as constant.

We vary ε and a , and evaluate the average number of TLR3-RNA bonds per RNA bundle, n_B . We also calculate the probability that no TLR3 attach to the RNA cluster: p_0 , with the subscript denoting zero bonds. This probability is proportional to the (cluster-membrane) dissociation rate, and hence, to the dissociation constant. The total number of bound clusters N is inversely proportional to the dissociation constant, therefore, neglecting TLR3 depletion and cluster steric repulsion: $N \propto 1/p_0$. The total number of bound (activated) receptors is proportional to the ratio: $N_A = n_B N \propto \frac{n_B}{p_0}$.

4. Supplementary Discussion

4.1 Structures of polycation-dsRNA complexes are mostly insensitive to changes to stoichiometry

The majority of the characterized polycation-dsRNA complexes did not exhibit significant changes in the first-peak positions across the wide range of tested peptide-to-dsRNA stoichiometric ratios (and by implication charge ratios), indicating that most of these structures are robust to changes in relative stoichiometry. Moreover, the LL37-dsRNA complex was found to be stable in human serum, which indicates that the self-assembly process is robust even in the presence of other proteins. Indeed, this is not unexpected on physics grounds: Electrostatic self-assembly at physiological conditions favors binding between components with equal and

opposite surface charge densities due to the resultant maximal entropy gain of counterion release (8), which is the case for dsRNA and LL37. However, a small subset of the tested peptide-dsRNA complexes (EF15 and LL34) exhibited a small shift in their first peak position from a lower to higher q as the peptide-to-dsRNA charge ratio increased from below the isoelectric point ($P/RNA = 1/4, 1/2$) to isoelectric ($P/RNA = 1/1$) and beyond ($P/RNA = 2/1, 4/1$). This behavior indicates that the structure of the complex is changing with stoichiometry. However, it is interesting to note that these data points also follow the basic trend line (Figure 1E)

4.2 Potential relationship between TLR3 activation and the inter-RNA spacing within dsRNA complexes

The potential structural criterion outlined above is an interesting finding, given that the prevailing paradigm of immune activation is that the spatial organization of dsRNA ligands is not expected to influence the magnitude of activation. To test the statistical significance of these trends, we construct a null hypothesis based on the assumption that there is no relationship between TLR3 activation (as measured by IL-6 secretion) and the inter-dsRNA spacing. The inter-dsRNA spacings (inversely proportional to first-peak position q) and the magnitude of TLR3 activation are assumed to be two random variables. That the present problem involves nonlinear correlations dictates that it is necessary to go beyond the usual linear statistical methods. To this end, we used the recently developed metric distance correlation (R_{dCor}) (9, 10) to quantify the association between our paired variables without assuming any functional form of the correlation (e.g. fitting the data parametrically to a function). By definition, R_{dCor} takes on values between 0 and 1. $R_{dCor} = 0$ if and only if the variables are statistically independent, while $R_{dCor} = 1$ if strongly dependent. Using a Monte-Carlo simulation ($N = 100,000$ sampling iterations), we randomly sampled the experimental dataset of measured IL-6 production for polycation-dsRNA complexes with the null hypothesis that there is no correlation between the structure of the complexes and IL-6 activation. We find that the distance correlation between the inter-dsRNA spacing and TLR3 activation is $R_{dCor} = 0.371$ [0.327, 0.492] with $P = 0.022$ at a 95% significance level of $\alpha = 0.05$ (Figure S1A), indicating a likely relationship between TLR3 activation and inter-RNA spacing. To test this finding further, we also calculated the recently developed maximal information coefficient (MIC), which non-parametrically measures the strength of the non-linear association between paired variables (11). Like $dCor$, MIC takes on values between 0 and 1. MIC values close to 0 indicate statistical independence while values near 1 indicate a strong functional relationship. Using a similar Monte-Carlo simulation ($N = 100,000$), we conducted a null-hypothesis significance test using MIC (12). The MIC correlation between inter-dsRNA spacing and TLR3 activation was $MIC = 0.652$ [0.414, 0.894] with $P < 10^{-5}$ at a 95% significance level of $\alpha = 0.05$ (Figure S1B). Taken together, these two results suggest that the null hypothesis is highly unlikely, and that there is clearly a statistically significant nonlinear relationship between TLR3 activation and the inter-RNA spacings of self-assembled RNA complexes.

5. Supplementary Figures

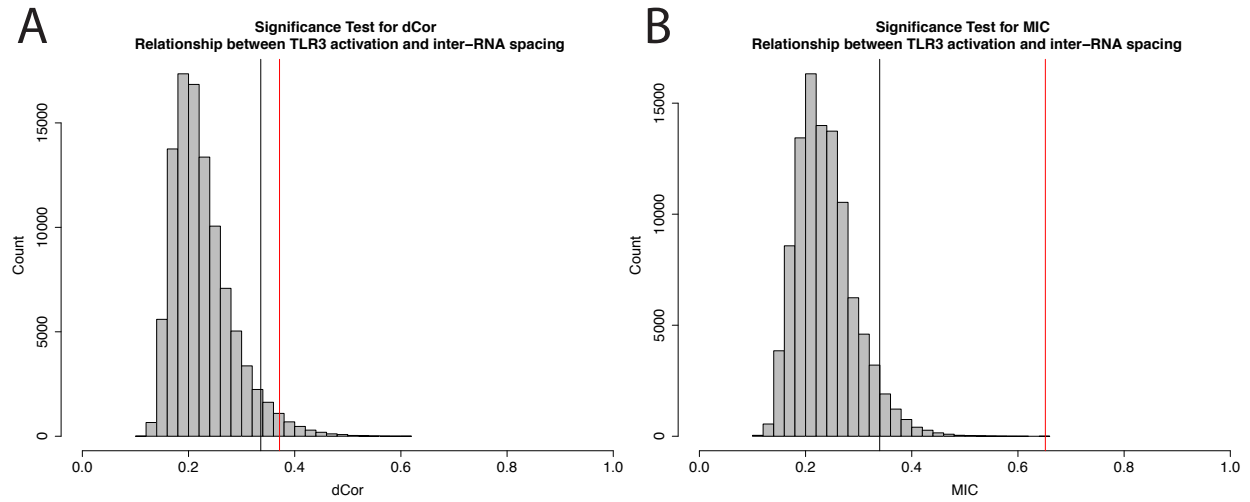


Figure S1: Null-hypothesis significance test for statistical dependence between TLR3 activation and inter-dsRNA spacing. (A) We calculated the distance correlation (dCor) between fold-increase in IL-6 production and inter-dsRNA spacing ($q = 2\pi/d$) for the 15 complexes (IL-6 measured in triplicate). Using 100,000 Monte-Carlo iterations with $N = 45$, we plot the null distribution and show our experimental findings relative to the significance threshold. We find that the observed dCor = 0.371 [0.327, 0.492] (vertical red line) exceeds the 95% significance level of $\alpha = 0.05$ (vertical black line) with $P = 0.022$. Analysis was done in R using the ‘energy’ package. (B) Using the same dataset, we did a null-hypothesis simulation test (100,000 Monte-Carlo iterations) for the maximal information coefficient (MIC), which also measures the strength of nonlinear correlations. We find that the MIC = 0.652 [0.414, 0.894] (vertical red line) also exceeds the 95% significance level of $\alpha = 0.05$ (vertical black line) with $P < 10^{-5}$. This indicates that it is unlikely that TLR3 activation and inter-RNA spacings are statistically independent, and that there is a clear relationship between the structure of crystalline RNA complexes and immune activation. Analysis was done in R using the ‘minerva’ package.

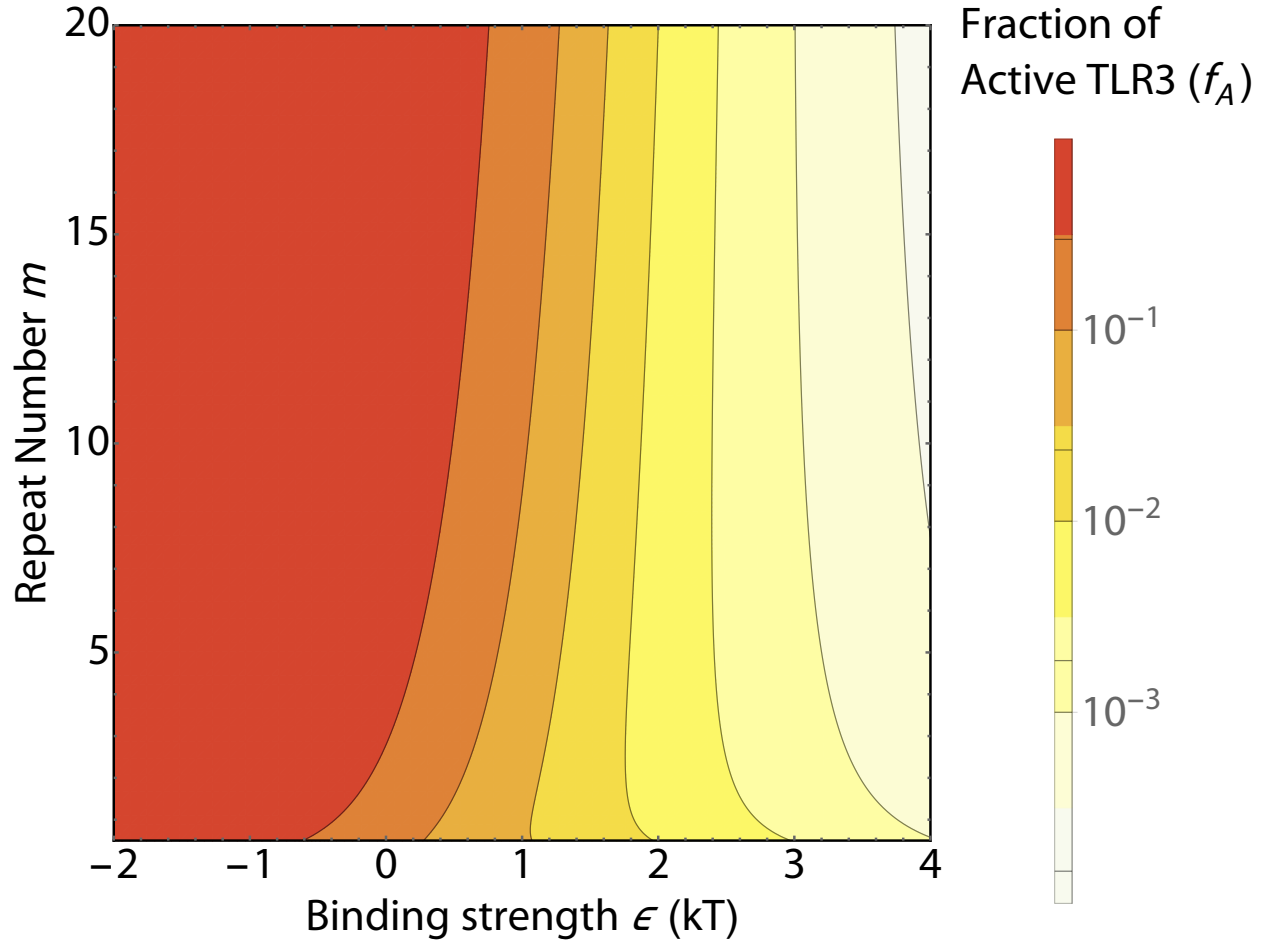


Figure S2: **Effects of repeat number m and binding strength ϵ on TLR3 binding to peptide-dsRNA nanocrystalline clusters.** Contour plot showing the fraction of active TLR3 receptors f_A as a function of the repeat number m and the binding strength ϵ (units of kT) for a single TLR3 binding to the nanocrystalline cluster. The prefactor was chosen as $C^*=10^{-3}$. changing the prefactor results in only minor quantitative differences. A similar figure in the main text (Figure 4B) shows the binding efficiency as a function of the repeat number m and the lattice spacing indicated by the first peak position q : $a=2\pi/q$. The binding strength depends on the inter-dsRNA spacing as specified by the Eqns. (4) and (5): $\epsilon = \epsilon^* + 2U(a)$. With the value $\epsilon^*=2k_B T$ chosen here, the optimal spacings correspond to negative values of ϵ (net attraction) while positive values of ϵ and net repulsion are indicating suboptimal spacings.

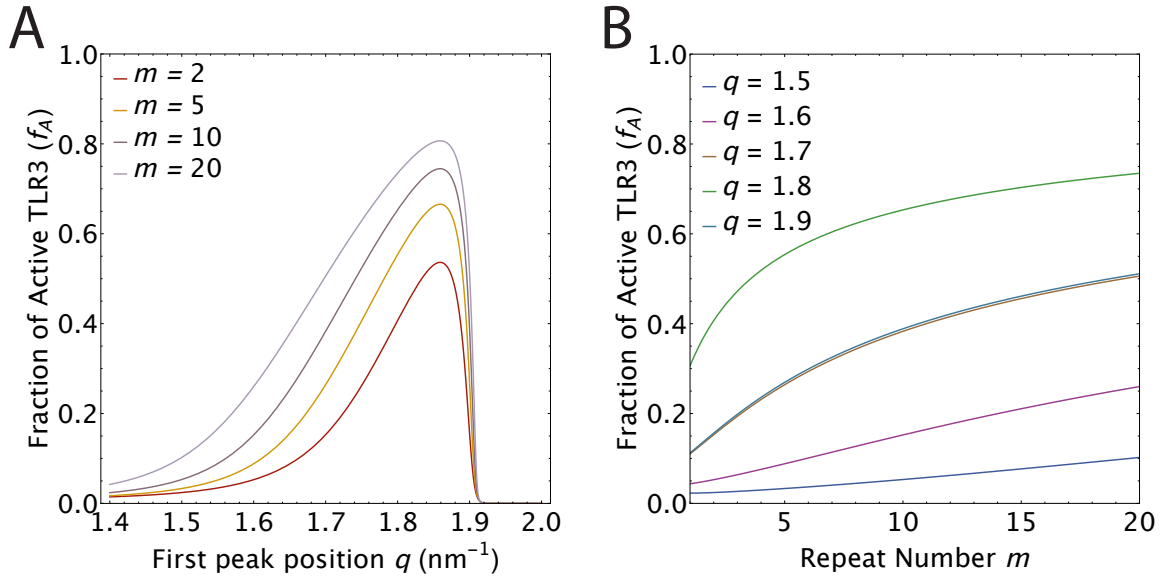


Figure S3: **Dependence of TLR3 activation on first peak position q and repeat number m .** (A) Slices taken from Figure 4B at constant values of repeat number $m = 2, 5, 10$, and 20 . The broadening of the peaks as m increases indicates that the range of inter-dsRNA spacings that can accommodate strong TLR3 activation increases as the size of the nanocrystalline cluster increases. For smaller clusters, the optimal range of spacings is more confined. For clusters near the optimal value of q , increase in m leads to a larger fraction of bound TLR3. (B) Slices taken from Figure 4B at constant values of inter-dsRNA spacings corresponding to $q = 1.5, 1.6, 1.7, 1.8$, and 1.9 nm^{-1} . Note that $q = 1.8 \text{ nm}^{-1}$ has a higher ceiling of bound TLR3 for a given repeat number compared to $q = 1.7$ or 1.9 nm^{-1} . The dependence is much stronger for clusters close to the optimal spacing ($q = 1.8 \text{ nm}^{-1}$), but weaker for those further away from the optimal spacing ($q = 1.5 \text{ nm}^{-1}$).

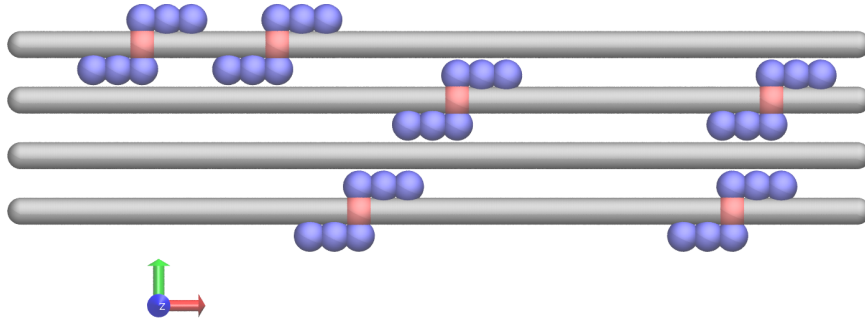


Figure S4: **Monte-Carlo simulation snapshot of TLR3 dimers binding to a dsRNA-AMP nanocrystalline cluster.** Parallel dsRNA within the crystal are shown as four grey rods. dsRNA binding TLR3 dimers are modeled as two blue paddles (each represented with 3 balls) connected by a red linker. The length of dsRNA rods is 50 nm and the size of each TLR3 paddle is 4.4 nm. For this snapshot, the spacing between dsRNA rods is commensurate with the steric size of TLR3 (such as with LL37-dsRNA), leading to a drastic amplification of bound receptors via a variation of the superselectivity mechanism.

6. References

1. Ilavsky J (2012) Nika: software for two-dimensional data reduction. *J Appl Crystallogr* 45(2):324–328.
2. Hammersley AP (1997) FIT2D: an introduction and overview. *European Synchrotron Radiation Facility Internal Report: ESRF97HA02T*.
3. DeRouchey J, Netz RR, Radler JO (2005) Structural investigations of DNA-polycation complexes. *Eur Phys J E* 16(1):17–28.
4. Schmidt NW, et al. (2015) Liquid-crystalline ordering of antimicrobial peptide-DNA complexes controls TLR9 activation. *Nat Mater* 14(7):696–700.
5. Warren BE (1941) X-Ray Diffraction in Random Layer Lattices. *Phys Rev* 59(9):693–698.
6. Needleman DJ, et al. (2004) Higher-order assembly of microtubules by counterions: from hexagonal bundles to living necklaces. *Proc Natl Acad Sci USA* 101(46):16099–16103.
7. Borkowski AW, Park K, Uchida Y, Gallo RL (2013) Activation of TLR3 in keratinocytes increases expression of genes involved in formation of the epidermis, lipid accumulation, and epidermal organelles. *J Invest Dermatol* 133(8):2031–2040.
8. Wong GCL (2006) Electrostatics of rigid polyelectrolytes. *Current Opinion in Colloid & Interface Science* 11(6):310–315.
9. Székely GJ, Rizzo ML, Bakirov NK (2007) Measuring and testing dependence by correlation of distances. *The Annals of Statistics* 35(6):2769–2794.
10. Székely GJ, Rizzo ML (2013) Energy statistics: A class of statistics based on distances. *Journal of Statistical Planning and Inference* 143(8):1249–1272.
11. Reshef DN, et al. (2011) Detecting novel associations in large data sets. *Science* 334(6062):1518–1524.
12. Albanese D, et al. (2013) Minerva and minepy: a C engine for the MINE suite and its R, Python and MATLAB wrappers. *Bioinformatics* 29(3):407–408.